ACS OMEGA

Open Access



http://pubs.acs.org/journal/acsodf

Article

# Numerical Modeling of Multiphysics Constitutive Relations Governing Water Migration into Variably Saturated Sorptive Shale

Kaifu Mi, Yingying Xu,* Yu Lei, Juncheng Wang, Pengyu Shen, and Xueming Zhang

Cite This: *ACS Omega* 2025, 10, 6948−6964

Read Online

ACCESS | Metrics & More | Article Recommendations

**ABSTRACT:** The water invasion within shales easily causes damage to the hydrocarbon flow. However, the water imbibition mechanisms are still unclear, and the mathematical connection between stress-dependent permeability and water imbibition was rarely known. As a result, in this paper, a numerical simulation model coupled with water imbibition, shale deformation, and shale permeability alteration was established to analyze how water imbibition lead to an alteration in geomechanical properties and shale gas permeability. The results showed that the proposed model was validated with the high pressure imbibition experimental data of shale samples. Moreover, more comprehensive water imbibition mechanisms included in the model can improve the prediction accuracy for the water imbibition process. Furthermore, the water imbibition distance was demonstrated to be a power function of water imbibition duration and clay mineral content, an exponential expression of initial matrix permeability, and a positively linear equation of the injection pressure difference. Last but not least, the elastic modulus after hydration is negatively related to matrix permeability, clay mineral content, and injection pressure difference. These bigger control factors will result in clay swelling and cementation weakening during the water imbibition, finally enhancing stress sensitivity and decreasing permeability. Finally, the cores with a high clay mineral content and injection pressure difference are likely to enhance stress sensitivity, obeying the positive power function and linear function, respectively. The findings can provide a scientific basis to study the water-sensitive damage to flow capacity and stress sensitivity for unconventional formations in a water environment.

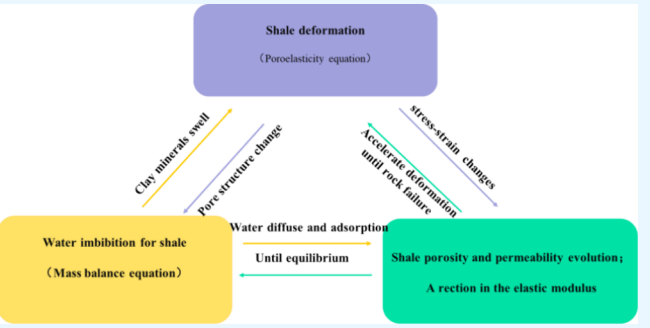


## 1. INTRODUCTION

Shale gas has gradually become an ideal alternative to fossil energy occurring in tight shale reservoirs as a result of its cleanliness.[1] Generally, the ultralow permeability and porosity geological characteristic makes it difficult to extract shale gas out of tight shale reservoirs, which seriously limits the gas extraction efficiently.[2] For this reason, horizontal drilling and hydraulic fracturing have become mainstream techniques to enhance shale gas production worldwide.[3] During the fracturing operations, a large volume of water-based working fluids is injected into the tight formations under high pressure conditions for the aim of creating cracks and unlocking tight resources.[4] However, field data indicates that a low flowback recovery of fracturing fluids[5] often takes place as the uncovered fluids will imbibe within the formations dominated by complex imbibition driving forces.[6]

Due to the abundant micronanopores in the shale rock, capillary pressure is known as the primary mechanism for fracturing fluid loss and low water recovery during and after the fracturing operation.[7] Capillary force has been defined as a function of rock wettability, pore radius, and interfacial tension, which makes it possible for a considerable amount of water infiltration into the shale gas reservoirs.[8,9] In addition, water-wet shale exhibits a strong adsorption to multilayered water molecules as a result of the presence of clay minerals.[10] Clay minerals can function as semipermeable membranes because of the negative charges on clay particle surfaces.[11,12] Moreover, the water invasion behavior in shale is controlled by the osmotic pressure as well, caused by the salinity difference between the fracturing fluid and the formation water until the salt concentration reaches equilibrium.[13] Many studies have been carried out on the water imbibition phenomenon and its mechanisms in unconventional reservoirs through experimental and theoretical analysis. In terms of experimental research. Li et al.[14] found that in the process of oil displacement, small pores imbibe water or chemical solution driven by capillary force, while large pores drive oil out of the pores by capillary forces between different pores. It indicated that wettability,

Received: October 24, 2024
Revised: January 3, 2025
Accepted: January 10, 2025
Published: February 16, 2025

experimental oil viscosity, and interfacial tension played an important role in the process of spontaneous imbibition. Pu et al.[15] analyzed the static imbibition mechanism in tight reservoir using the NMRI technique. They obtained the nuclear magnetic resonance T2 relaxation spectrum of the imbibition process to monitor the change of oil in the core pores, and they thought that the aqueous solution preferentially entered the small pores during imbibition. Akin and Kovscek[16] carried out the countercurrent imbibition experiment for simulating water imbibition and air displacement with diatomite and Berea sandstone and observed the changes of the imbibition front in the two groups of experiments with a CT scanner. Wang and Yang[17] simulated the imbibition of three tight sandstone cores of Yanchang Formation in the Ordos basin with different pore distributions to compare the pore distribution of each core and its imbibition displacement rate. In addition, the numerous theoretical works reported the development and application of analytical and numerical solutions for water imbibition.[18,19] Wang et al.[20] proposed an imbibition model based on the capillary tube model and obtained that the maximum imbibition distance decreased first and then increased with the pore radium increasing from 1 to 200 nm. Wang and Zhao[21] characterized the water imbibition process into oil-saturated tight sandstones using a semianalytical model of characterizing based on the capillary tube model and fractal theory. Salam and Wang[22] derived a new analytical model of spontaneous imbibition heights in low-permeability reservoirs considering effective viscosity, surface roughness, slip, and gravity effects in a single tortuous capillary tube. Shun et al.[23] built an oil−water two-phase flow mathematical model in a dual-porous and dual-permeable media with taking the effect of imbibition into consideration. Tavassoli et al.[24] presented an expression for the saturation profile and analyzed oil recovery during countercurrent imbibition from a strongly water-wet system. Behbahani et al.[25] carried out countercurrent imbibition simulations in water-wet fractured reservoirs. In summary, many researchers have conducted research on the spontaneous imbibition phenomenon. However, the core-scale imbibition experiment might represent the water imbibition characteristic for certain geological formations, and more importantly, we cannot accurately evaluate the water imbibition tendency for a longer time using the experimental approaches for the sake of financial support and investment time. For this reason, numerical simulation has become a preferential alterative for predicting the water imbibition for shale at different conditions. From the literature review of the predecessors' numerical simulation work, they have mainly established imbibition models either for capillary tubes or conventional porous media. Instead, numerical simulation works for water imbibition within unconventional shale gas reservoirs are rarely seen. More importantly, the traditional models did not consider fully water imbibition mechanisms, primarily focusing on capillary pressure, even though the water adsorption induced by the clay minerals and osmosis pressure dominated by the salinity difference both are demonstrated to be crucial for the water imbibition process. It will lead to an obvious inaccuracy in the prediction results of the water imbibition process.

Many previous studies have attempted to confirm that the water-based working fluid imbibition has presented some engineering challenges to the mechanical characteristics of shale, such as borehole wall instability induced by hydration damage, affecting the propagation of hydraulic fractures.[26] Since the clay minerals in shale mainly contain microscale pores, water prefers to occur in clay minerals as a fully or partially adsorbed phase rather than a bulk phase,[27] causing clay minerals to swell and further leading to changes in the local internal stress.[28] The clay-swelling-induced internal stress results in the reduction of pore pressure and increase in effective pressure, which enhances the permeability stress sensitivity and further blocks the fluid migration in the reservoir.[29] Moreover, it will weaken the cementing strength between rock clay particles and further lead to the reduction in the mechanical strength and elastic modulus of rocks, which finally triggers shale deformation during the gas depletion and geomechanical property change.[30] It is detrimental to long-term gas production. Thus, it is necessary to better understand the impact of water-based working fluid imbibition on the alteration in both shale dynamic geomechanical behavior and stress-dependent permeability. Up to date, several numerical simulations are generally applied to study the coupled multiphysical processes, linking the water imbibition to the rock deformation. A microcrack model based on the subcritical damage laws was proposed to describe the deformation and damage of brittle rock.[31,32] A micromechanics-based numerical model was used to examine the time-dependent microcrack growth.[33] The classical micromechanical model combined with the subcritical microcrack growth was used to describe the deformation behavior of water-saturated rocks.[34] Although the available publications provide clear evidence that spontaneous water-based working fluid imbibition has a great influence on the mechanical properties of shale, the effect of clay swelling on water imbibition and shale gas stress-dependent permeability, coupled with the geomechanical field for shale reservoirs, was not fully considered in the above models. Moreover, the experimental conclusions and numerical simulations for water imbibition are not effectively combined.

To fill these gaps, with the water imbibition mechanisms of water adsorption, capillary pressure, and osmosis pressure taken into account, a numerical simulation model coupled with multiphysics processes including water imbibition, shale deformation, and shale permeability alteration was established, and a calculation procedure by the finite difference method was proposed to efficiently compute this model. In addition, the experimental data on the shale core under high pressure water imbibition conditions was used to validate the proposed simulation model. Moreover, the water spatial distribution under shale deformation conditions was investigated. Moreover, the impact of water retention on shale matrix clay swelling and stress sensitivity parameters was further mathematically explored. The findings provided a theoretical basis for clarifying stress-sensitive damage for clay-rich shale gas reservoirs attributed to fluid imbibition.

## 2. MODEL DEVELOPMENT

**2.1. Water Imbibition Mechanisms.** *2.1.1. Capillary-Driven Mechanism.* The capillary force in the abundant nanomicropores controls the migration of fracturing fluid within the deeper reservoir, further affecting the production of the gas well. Therefore, the capillary force is significant in the imbibition process. According to the Young−Laplace law, as shown in Figure 1, the capillary force depends on the surface tension $\sigma$, the contact angle $\theta$, and the capillary radius $r$, which can be written as eq 1:



https://doi.org/10.1021/acsomega.4c09681
ACS Omega 2025, 10, 6948−6964

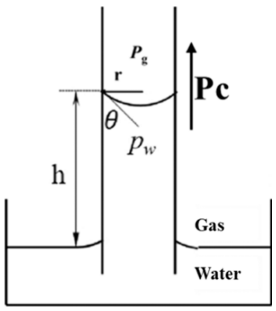


**Figure 1.** Liquid level rise due to capillary force.

$$p_c = \frac{2\sigma \cos\theta}{Ar} \quad (1)$$

where $p_c$ represents the capillary pressure, Pa; $\sigma$ represents the surface tension at the wetting phase and rock interface, N·m;$\theta$ represents the contact angle; $A$ represents the contact surface area, $m^2$; $r$ represents the pore radius, m.

*2.1.2. Osmosis-Driven Mechanism.* The capillary force in the reservoir occurs instantaneously, while the osmotic hydration takes a longer time in the imbibition process. During the fracturing process, chemical osmotic pressure is generated to induce water molecules to pass from the low-salinity solution to the high-salinity solution through the semipermeable membrane to achieve a salinity balance, as indicated in Figure 2. Chemical osmotic pressure is closely related to the clay semipermeable membrane efficiency and the difference in ion concentration. The membrane efficiency is used to describe the ability of a semipermeable membrane to restrict the passage of charged particles, ranging from 0 (no membrane) to 1 (ideal membrane). The higher the efficiency of the reservoir membrane, the greater the number of ions passing through the semipermeable membrane. However, naturally, most semipermeable membranes exhibit non-idealities, a sufficiently thick and well-compacted clay mineral layer will result in a membrane efficiency value close to 1, and the membrane efficiency will change with concentration. In this study, we assume that the effective permeability coefficient remains constant and does not change with concentration. The membrane efficiency of shale reservoirs mostly ranges from 0.1 to 0.3. The osmotic pressure can be described by the following formula (see eq 2):[35]

$$p_\pi = n\frac{RT}{\overline{V}_w} \ln \frac{x_1}{x_2} \quad (2)$$

(a) $x_1 < x_2$, osmotic pressure causes water in the fracturing fluid to enter the shale, causing the water content within the shale to increase;
(b) $x_1 = x_2$, water imbibition without osmotic pressure;
(c) $x_1 > x_2$, osmotic pressure promotes water within the shale to flow out, causing the water content of the shale to decrease.

where $p_\pi$ represents the osmosis pressure, Pa; $R$ is the ideal gas constant, 8.314 J/(mol·K); $\overline{V}_w$ represents the water mole volume, $18.02 \times 10^{-6}$ $m^3$/mol; $T$ represents the temperature, K; $x_i$ is the water activity for solution $i$ ($i$ = 1, 2), dimensionless; $n$ is the semipermeable membrane efficiency, dimensionless.

Substitute the concentration difference into the osmosis pressure, eq 2 can be rewritten as eq 3:

$$p_\pi = nvRT(c_2 - c_1) \quad (3)$$

where $c_i$ is the solution concentration for solution $i$ ($i$ = 1, 2), mol/$m^3$; $v$ is the number of ions contained in an electrolyte solution, dimensionless.

*2.1.3. Water Adsorption Mechanism.* Under certain geological environments, clay mineral hydration is used to characterize the ability of clay minerals to adsorb water molecules. The water adsorption to clay mineral process consists of surface hydration and osmosis hydration for inorganic pores. Surface hydration is caused by the adsorption of water molecules and exchangeable cation hydration on the clay crystal surface (expansive clay surface includes the outer surface and inner surface). The hydrogen and hydroxyl functional groups on the surface of clay can form hydrogen bonds with water molecules, thereby adsorbing water molecules to the surface of clay crystals. There is a direct relationship between the surface hydration of clay minerals and the crystal layer expansion.[36] In clay mineralogy, multilayer water adsorption is often used to describe the surface hydration ability.[37] The number of layers of adsorbed water molecules between clay mineral crystal layers is closely related to the relative humidity. That is, the layer of water molecules between clay mineral layers will increase discontinuously (stepwise) as the relative humidity increases. It can be increased to up to four layers of water molecules, corresponding to a layer spacing of 2.2 nm.[38] Meanwhile, the clay swelling pressure will also decrease with the increase in the number of layers of water molecules.[39] Osmotic hydration refers to the concentration of cations between crystal layers being greater than the solution concentration, causing the

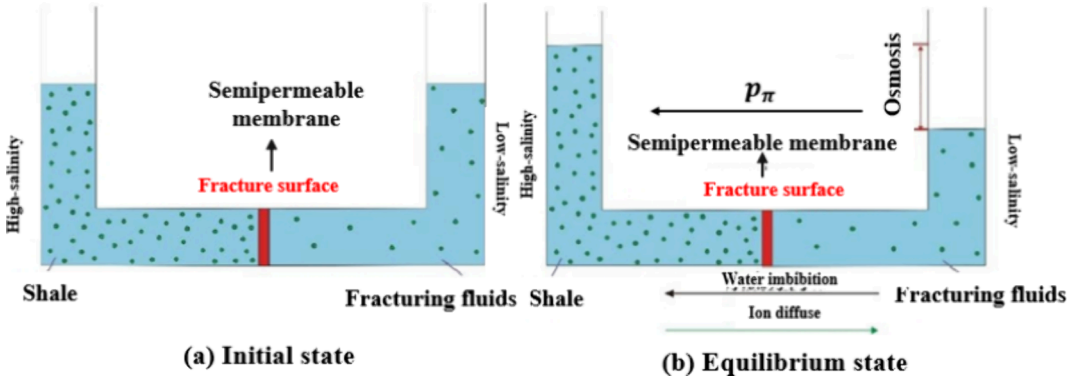


**Figure 2.** (a, b) Aqueous phase migration and ion diffusion processes dominated by osmotic pressure.



https://doi.org/10.1021/acsomega.4c09681
ACS Omega 2025, 10, 6948−6964

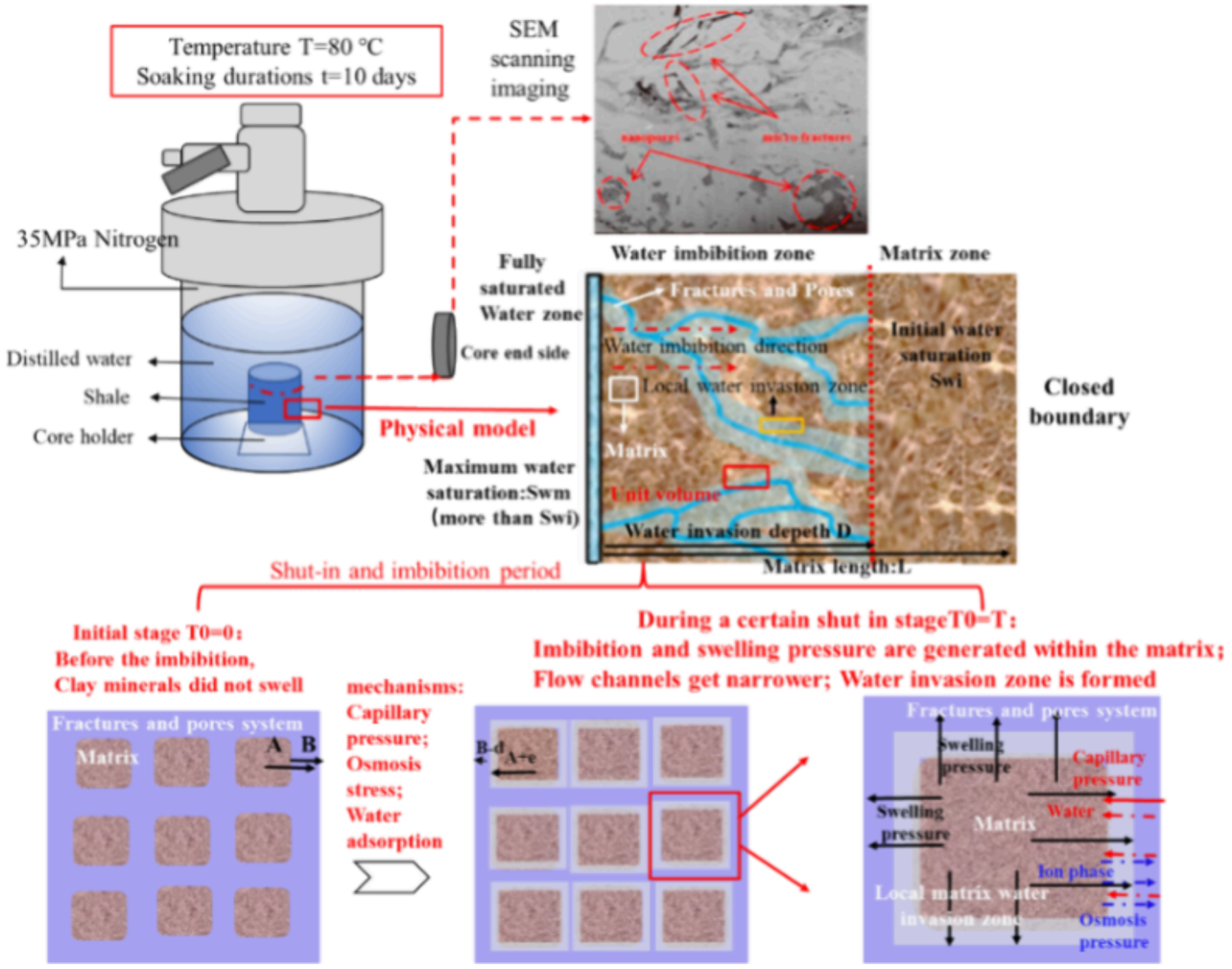


**Figure 3.** One-dimensional numerical simulation for water imbibition into a shale matrix.

cations to form fully hydrated cations, which will fall off the surface of the clay mineral and form a tendency to diffuse into the solution. At the same time, hydrated cations are attracted by the electrostatic attraction on the surface of clay minerals and finally show a dynamic equilibrium state, forming a diffusion double electric layer. Therefore, the cations between the clay crystal layer structures will trigger a hydration phenomenon under action of osmotic pressure and electric double layer repulsion, which will push the clay mineral crystal layers away from each other, causing the distance between the clay mineral layers to increase sharply. The resulting osmotic expansion will be much greater than the lattice expansion, eventually leading to separation of the crystal layers and a significant increase in the macroscopic volume of the clay minerals. The hydration degree of clay minerals is usually characterized quantitatively by using an isothermal adsorption model. It is assumed that under the low coverage rate of water molecules on the surface of clay minerals, water molecules are first adsorbed on the main adsorption sites of clay minerals according to the Langmuir principle, and then, the second layer of adsorbed water molecules covers a layer of already adsorbed molecules.

Taking into account the expansion phenomenon caused by clay hydration and considering that the expansion capacity is proportional to the clay minerals content, the mathematical model of multilayer adsorption of water molecules in clay minerals is obtained as eq 4:[40]

$$m_w = \frac{x_c \rho_s m_L R_h}{(R_h + R_L)(1 - cR_h)} \tag{4}$$

where $m_w$ is the adsorbed water volume per unit mass of rock at a specific relative humidity, $cm^3/g$; $x_c$represents the clay mineral content, dimensionless; $m_L$ indicates the local adsorption capacity when the entire adsorbent surface is completely covered by a monolayer, g/g; $\rho_s$ is the rock density, $g/cm^3$; $c$ is related to the net heat of adsorption, dimensionless; $R_h$ is the relative humidity, dimensionless; $R_L$ is the relative humidity corresponding to when 50% of the adsorbent surface is covered by a monolayer, dimensionless.

*2.1.4. Injection Pressure Difference Mechanism.* During the fracturing process, the fracturing fluid imbibes into rock cracks and pores under the action of the injection pressure difference, which is defined as the pressure difference between the inlet pressure of the external fracturing fluid and the gas pressure in the reservoir. The expression is described as eq 5:

$$p_d = p_{w0} - p_g \tag{5}$$

where $p_d$ represents the injection pressure difference, Pa; $p_{w0}$ represents the water injection pressure at the end side of core, Pa; $p_g$ is the gas pressure, $Pa_o$.



https://doi.org/10.1021/acsomega.4c09681
ACS Omega 2025, 10, 6948−6964

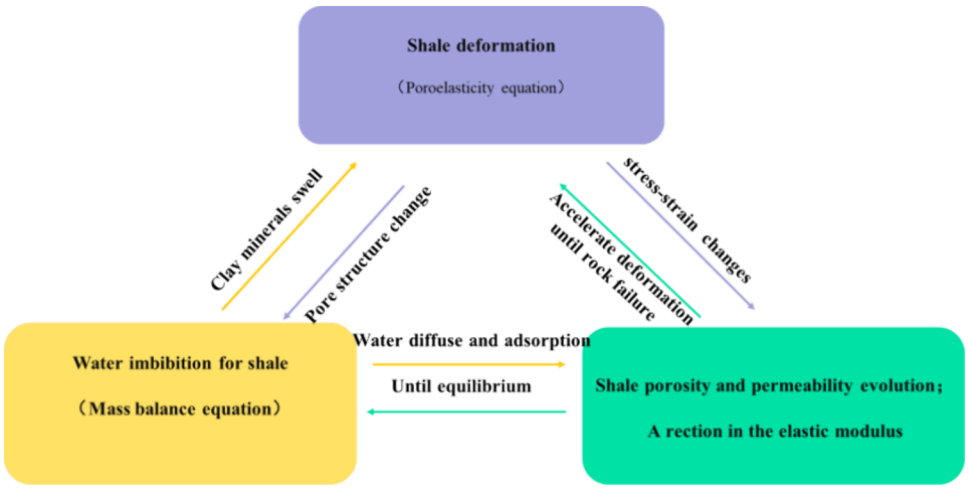


**Figure 4.** Description of the coupling relationships of the multiphysics processes.

**2.2. Governing Equations.** *2.2.1. Water Imbibition.* As described in Figure 3, when the fracturing fluid is driven by imbibition forces such as capillary force, chemical osmotic pressure, injection pressure difference, and water adsorption, it will occupy the microfractures and micronanopores within shale. Consequently, a water invasion zone is formed near the imbibition end face. In this area, water imbibition and subsequent water−rock interaction will lead to changes in mechanical properties. In addition, it causes swelling stress in clay minerals, further affects the stress field in the invasion zone, which finally induces the hydrated matrix deformation, and causes serious stress sensitivity. Therefore, it is critical to understand that the shale matrix imbibition phenomenon is a multiphysical process involving the water phase seepage field and geomechanical field for shale deformation.

In this section, the numerical simulation composed of water imbibition, shale deformation, and shale permeability alteration was set up. The governing equation for the water imbibition took into account three main mechanisms including the capillary-driven, osmosis-driven, forced imbibition-driven, and adsorption-driven imbibition.[41] The shale micro/nanopores dominate capillary-driven imbibition process in which the capillary pressure is usually high,[42] while the osmotic-driven imbibition occurs when shale membranes separate the low-concentration fracturing fluid and the high-concentration strata water. In addition, the adsorption-driven mechanism mainly takes place in the clay minerals inside shale. The shale deformation constitutes the geochemical governing equations contributing to the clay swelling after the water adsorption. The third governing equation describes the permeability changes that are sensitive to the effective stress after water imbibition.

We coupled these multiphysics processes as briefly depicted in Figure 4. Water imbibition results in the clay mineral swelling and further cause shale deformation. Likewise, shale deformation triggers changes in the stress−strain state and leads to the alteration in shale dynamic porosity−permeability. Meanwhile, changes in shale properties caused by shale deformation ultimately affects shale deformation and water spontaneous imbibition.

To simplify the solution process, the basic assumptions for establishing the physical model were as follows: (1) The selected unit is a homogeneous and isotropic matrix core, which obeys the poroelastic theory without considering the bedding effect; (2) The shale deformation is consistent with the small deformation hypothesis, and the water phase adsorption only occurs on the surface of clay minerals; (3) Considering the one-dimensional imbibition process, and isothermal seepage is approximately considered to be instantaneous, the fluid diffusion conforms to Darcy's law; (4) Compared with capillary pressure and osmotic pressure, gravity has a relatively smaller impact on the imbibition effect, which can be ignored in the model; (5) The only formation water component considered in this model is common NaCl brine.

The initial water saturation and salinity are, respectively, $S_{w0}$ and $c_0$. The maximum water saturation at the inlet of the imbibition end is regarded as $S_{wm}$, and the salinity of the fracturing fluid at the inlet is 0. The matrix length is $L$, the imbibition cross-sectional area is $A$, and the water invasion zone width is $D$.

(1) The flow governing equations for the water phase

Based on the mass conservation equation, Darcy's equation, and van't Hoff's law,[43] considering the capillary pressure, osmotic pressure, water adsorption, and injection pressure difference, the continuity equation for water phase imbibition within the matrix unit can be obtained in eq 6:

$$\frac{\partial(\rho_w S_w \phi)}{\partial t} + \frac{\partial(x_c m_w)}{\partial t} = \frac{\partial}{\partial x}\left(-\rho_w \frac{k k_{rw}}{\mu_w} \frac{\partial(p_w - p_\pi - p_d)}{\partial S_w} \frac{\partial S_w}{\partial x}\right) \quad (6)$$

where $\rho_w$ is the water phase density, we regard it as 1 g/cm$^3$ in this model; $S_w$ represents the water saturation within the core, dimensionless; $\varphi$ indicates the core matrix porosity, dimensionless; $x_c$ represents the clay mineral content in the matrix, dimensionless; $m_w$ is the adsorption capacity of matrix clay minerals to the water phase under certain temperature and pressure conditions, g/cm$^3$; $k$ represents the shale matrix permeability, mD; $k_{rw}$ is the water phase relative permeability for the shale matrix, dimensionless; $\mu_w$ is the water phase viscosity under a certain geological conditions, Pa·s; $p_w$ represents the water phase pressure, Pa; $p_\pi$ represents



https://doi.org/10.1021/acsomega.4c09681
ACS Omega 2025, 10, 6948−6964

the osmosis pressure, Pa; $p_d$ represents the injection pressure difference, Pa.

The imbibition driving forces are calculated as in eq 7:

$$p_t = p_c + p_a + p_d \tag{7}$$

where $p_t$ is the total driving forces in the imbibition process, Pa; $p_c$ represents the capillary pressure, Pa.

There is also a logarithmic relationship between the total imbibition driving forces and the relative humidity, which can be expressed as eq 8:[44]

$$p_t = -\frac{RT}{v_{w0}M_w}\ln(R_h) \tag{8}$$

where $v_{w0}$ is the water phase specific surface, $cm^3/g$; $M_w$ is the molar mass of water vapor, g/mol.

$$p_c = \frac{2\sigma\cos\theta}{Ar} \tag{9}$$

$$p_\pi = nvRT(c - c_f) \tag{10}$$

where $c$ is the concentration of formation water in the matrix, mol/L; $c_f$ is the fracturing fluid concentration, mol/L, and it is assumed here to be 0.

Assuming that the relative permeabilities of both gas and water phases are functions of their respective saturations, the curve follows the Brooks−Corey model:[42]

$$K_{rg} = K_{rgd}\left(1 - \frac{S_w - S_{gr}}{1 - S_{gr} - S_{wr}}\right)^{n_g} \tag{11}$$

$$K_{rw} = K_{rwd}\left(\frac{S_w - S_{wr}}{1 - S_{gr} - S_{wr}}\right)^{n_w} \tag{12}$$

where $K_{rgd}$ is the end point of gas relative permeability, dimensionless; $K_{rwd}$ is the end point of water relative permeability, dimensionless; $S_{gr}$ is the residual gas saturation; $S_{wr}$ is the residual water saturation; $n_w$ is the water phase Corey index; $n_g$ is the gas phase Corey index.

The gas and water phases satisfy the following constraints:

$$S_w + S_g = 1 \tag{13}$$

where $S_g$ is the gas saturation, dimensionless.

(2) The flow governing equations for the salt phase

Based on the mass conservation equation and Van't Hoff's law,[43] the continuity equation of the salt in the matrix unit can be derived considering the solute diffusion and laminar flow, as well as the osmotic pressure:

$$\frac{\partial(cS_w\phi)}{\partial t} = \frac{\partial}{\partial x}[(1-n)\phi D_0\frac{\partial c}{\partial x}] - \frac{\partial}{\partial x}[(1-n)c\frac{kk_{rw}}{\mu_w}\frac{\partial(p_w - p_a - p_d)}{\partial S_w}\frac{\partial S_w}{\partial x}] \tag{14}$$

Due to the extremely low permeability of shale, the significance of convective flow is much smaller than that of diffusion, and further, the convective flow can be ignored. Therefore, the ion diffusion is only considered in the model and the motion equation is usually written as

$$\frac{\partial(cS_w\phi)}{\partial t} = \frac{\partial}{\partial x}[(1-n)\phi D_0\frac{\partial c}{\partial x}] \tag{15}$$

where $c$ is the fracturing fluid concentration with the core matrix, mol/L; $D_0$ represents the intrinsic diffusion coefficient for ions of solutions, $m^2/s$.

(3) Auxiliary equations

To solve nonlinear equations such as gas−water two-phase flow, a series of auxiliary equations are established. Since the formation is considered to be elastic, the microcompressibility of the matrix needs to be coupled in the model. Therefore, the stress-sensitive equations of porosity and permeability can be expressed as eqs 16 and 17:

$$\varphi = \varphi_0\exp(-c_p(p - p_0)) \tag{16}$$

$$k = k_0\exp(-3c_p(p - p_0)) \tag{17}$$

where $\varphi_0$ is initial matrix porosity, dimensionless; $k_0$ is the initial matrix permeability, mD; $c_p$ is the compressibility coefficient for matrix pores, $Pa^{-1}$; $p$ is the matrix pore pressure, Pa; $p_0$ is the initial matrix pore pressure, Pa.

(4) Initial and boundary conditions

During the initial stage of matrix imbibition, the salinity, pore pressure, and water saturation everywhere inside the matrix are the same as their initial values.

$$S_w(t = 0) = S_{w0} \tag{18}$$

where $t$ represents the imbibition duration, s; $S_{w0}$ is the initial water saturation within the matrix, dimensionless.

$$c(t = 0) = c_0 \tag{19}$$

where $c_0$ is the initial ion concentration for fracturing fluids within the core matrix, mol/L.

$$p(t = 0) = p_0 \tag{20}$$

Outer boundary conditions:

It is assumed in the model that the exit end of the core is closed, so there is no mass exchange between the concentration and water saturation in the matrix and the outside, then

$$\frac{\partial c}{\partial x}|_{x=L} = 0 \tag{21}$$

$$\frac{\partial S_w}{\partial x}|_{x=L} = 0 \tag{22}$$

where $x$ is the position within the matrix away from the imbibition end side, m.

Internal boundary conditions:

The concentration and saturation of the matrix inlet end and the fracturing fluid are continuous, then

$$c(x = 0) = 0 \tag{23}$$

$$S_w(x = 0) = S_{wm} \tag{24}$$

where $S_{wm}$ is the maximum water saturation at the imbibition end for the cores, dimensionless.



https://doi.org/10.1021/acsomega.4c09681
ACS Omega 2025, 10, 6948−6964

*2.2.1.1.1. Geomechanical Model Considering Clay Swelling.* For porous media such as shale in the imbibition stage, the clay mineral swelling caused by the adsorption of water molecules has a non-negligible impact on the total strain. Assuming that the expansion caused by water adsorption is isotropic,[45] the strain caused by adsorption is incorporated into the stress−strain equation of a homogeneous and isotropic porous medium. It is stipulated that the reservoir pressure is positive, and then, based on poroelasticity theory, the stress−strain relationship can be expressed as eq 25:

$$\varepsilon_{ij} = \frac{1}{2G}\left(\sigma_{ij} - \frac{\sigma_{kk}\delta_{ij}}{3}\right) + \frac{\sigma_{kk}\delta_{ij}}{9K} - \frac{\alpha p}{3K}\delta_{ij} + \frac{\varepsilon_s}{3}\delta_{ij} \tag{25}$$

In eq 25, the first term on the right side of eq 25 represents the shear deformation strain caused by deviatoric stress, which does not change the volume of the porous medium; the second term is the volume strain caused by normal stress; and the third and fourth terms are the volumetric strains caused by pore pressure and adsorption expansion of water molecules, respectively. The above volume deformation only affects the volume of porous media without causing shear deformation.

$$G = \frac{E}{2(1+\nu)} \tag{26}$$

$$K = \frac{E}{3(1-2\nu)} \tag{27}$$

where $\varepsilon_{ij}$ refers to the total strain tensor, dimensionless; $\sigma_{ij}$ indicates the total stress tensor, dimensionless; $G$ means the shear modulus, Pa; $K$ indicates the volume modulus, Pa; $p$ represents the pore pressure, Pa; $\alpha$ represents the Biot coefficient, dimensionless; $\sigma_{kk}$ is the matrix geological normal stress, dimensionless; $\delta_{ij}$ represents the Kronecker coefficient: if $i = j$, the value is equal to 1; if $i \neq j$, the value means 0; $E$ represents the elastic modulus for the hydrated shale matrix, Pa; $\nu$ is the Poisson's ratio of the core matrix, dimensionless.

Considering that the impact of shale imbibition on the elastic modulus and the hydration change of rock Poisson's ratio is negligible, the hydrated core elastic modulus can be expressed as eq 28:

$$E = E_0 \exp\left(-x_c \frac{m_L R_h}{(R_h + R_L)(1 - cR_h)}\right) \tag{28}$$

where $E_0$ is the initial matrix elastic modulus of the core before hydration, Pa.

According to the multilayer adsorption of water molecules on the surface of clay minerals, the mathematical equation of clay swelling strain under any geological pressure can be derived as eq 29:

$$\varepsilon_s = x_c \frac{\varepsilon_L R_h}{(R_h + R_L)(1 - cR_h)} \tag{29}$$

where $\varepsilon_L$ is the maximum swelling strain when the entire adsorbent surface is completely covered by a monolayer, dimensionless; $\varepsilon_s$ refers to the matrix hydration swelling strain, dimensionless.

Since the gas and water both exist in the shale matrix during imbibition, the pore pressure not only depends on the two-phase pressure but is also closely related to the saturation.

$$p = p_w S_w + p_g S_g \tag{30}$$

where $p_g$represents the pore pressure within the matrix, Pa; $S_g$ is the gas saturation in the matrix pores, dimensionless.

Considering that the strain is very small, the volumetric strain is equal to the sum of the principal strains in the three directions: $\varepsilon_v = \varepsilon_{11} + \varepsilon_{22} + \varepsilon_{33}$. The volumetric strain caused by the deviatoric stress in the first term on the right side of eq 25 is 0; The external normal stress of the second term, also called the average compressive stress$\sigma = \frac{\sum_{i=1}^{3}\sigma_{ii}}{3} = \frac{\sigma_{11}+\sigma_{22}+\sigma_{33}}{3}$, generating the volumetric strain component $\frac{\sigma}{K}$; The volumetric strain component caused by the pore pressure of the third term is $-\frac{\alpha p}{K}$; The matrix swelling strain caused by the fourth term is $\varepsilon_s$. Therefore, the total volume strain of the matrix considering the adsorption expansion of water molecules can be expressed as

$$\begin{aligned}\varepsilon_v &= \varepsilon_{11} + \varepsilon_{22} + \varepsilon_{33} \\ &= \frac{\sigma}{K} - \frac{\alpha P}{K} + \varepsilon_s \\ &= \frac{1}{K}(\sigma - \alpha P + \varepsilon_s)\end{aligned} \tag{31}$$

It can be seen from eq 31 that the volume strain increases with the swelling strain and is negatively correlated with the pore pressure.

According to the effective stress criterion of porous media, considering the hydration expansion of the matrix, the effective stress can be expressed as[46]

$$\sigma_{ij}^{e} = \sigma_{ij} - (\alpha p - K\varepsilon_s)\delta_{ij} \tag{32}$$

The constitutive relationship of its linear elastic deformation can be expressed as follows:

$$\sigma_{ij} = 2G\varepsilon_{ij} + \left(K - \frac{2G}{3}\right)\varepsilon_{kk}\delta_{ij} + \alpha p\delta_{ij} - K\varepsilon_s\delta_{ij} \tag{33}$$

Combining eq 25 to eq 33, we can get the mathematical equation of effective stress−strain for shale matrix swelling deformation, which can be described by elastic modulus and Poisson's ratio:

$$\sigma_{ij}^{e} = \sigma_{ij} - \alpha p\delta_{ij} = \frac{E}{1+\nu}\left(\varepsilon_{ij} + \frac{\nu}{1-2\nu}\varepsilon_v\delta_{ij}\right) - K\varepsilon_s\delta_{ij} \tag{34}$$

Based on Cauchy's equation,[47] the relationship between total strain and matrix displacement can be established:

$$\varepsilon_{ij} = \frac{u_{i,j} + u_{j,i}}{2} \tag{35}$$

where $\lambda = K - \frac{2G}{3}$ is the Lame constant; $u$ is the displacement of a certain point on the matrix solid that changes with the imbibition time, m.

The equilibrium equation of shale can be expressed as[48]

$$\sigma_{ij,j} + f_i = 0 \tag{36}$$

where $f_i$ represents the volume force vector attached to the surface of the matrix, Pa/m. The subscript after the comma indicates the derivation of the coordinates in a certain direction, and the repeated indicators in the same single item indicate the traversal summation of the indicators.

Combining eqs 32−35, the Navier-type equation (eq 37) can be obtained as follows:



https://doi.org/10.1021/acsomega.4c09681
ACS Omega 2025, 10, 6948−6964

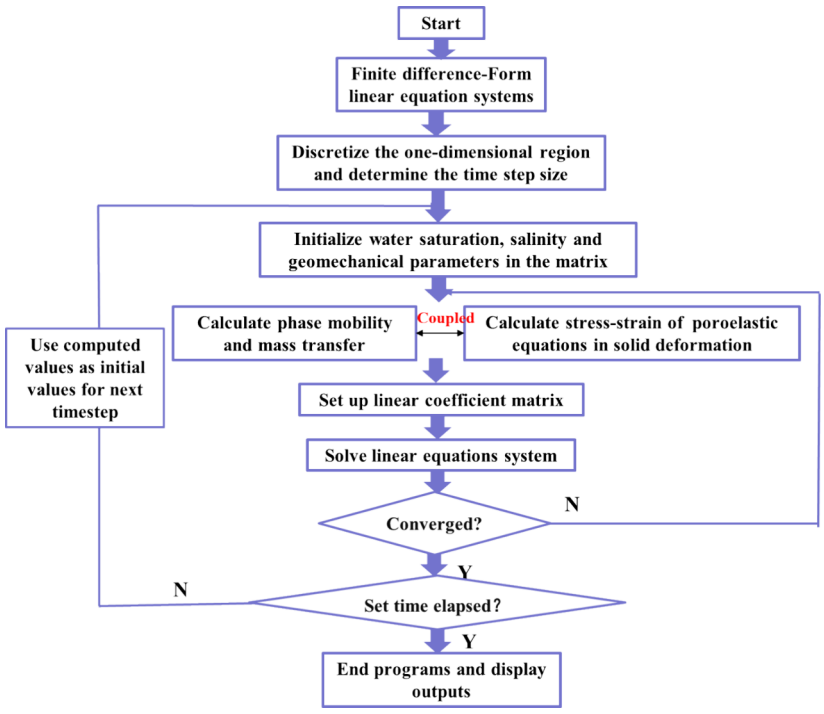


**Figure 5.** Iterative solution process for numerical simulation.

$$Gu_{i,jj} + \frac{G}{1-2v}u_{k,kj} - \alpha p + K\varepsilon_s + f_i = 0 \tag{37}$$

The above equation (eq 37) is the governing equation of shale matrix deformation coupled with the clay hydration expansion.

*2.2.1.1.2. Matrix Stress-Sensitive Permeability Model.* For overpressure, low-porosity, and low-permeability shale reservoirs, the imbibition process can easily change the stress field, lead to rock deformation, and affect the porosity and permeability of the rock. Therefore, the matrix permeability and matrix expansion deformation are directly related to the effective stress.

The apparent volume $V_b$ of the matrix system is divided into two parts, namely, the total pore volume within the matrix $V_p$and the closed pore volume without solid particles $V_s$:

$$V_b = V_p + V_s \tag{38}$$

The terms $\frac{dV_b}{V_b}$ and $\frac{dV_p}{V_p}$ are introduced to characterize the matrix apparent volume and pore volume strain change:

$$d\varepsilon_v = -\frac{dV_b}{V_b} = \frac{1}{K}(d\sigma - \alpha\, dp) + d\varepsilon_s \tag{39}$$

$$d\varepsilon_p = -\frac{dV_p}{V_p} = \frac{d\sigma}{K_p} - \frac{dp}{K_p}\left(1 - \frac{K_p}{K_s}\right) + d\varepsilon_s \tag{40}$$

where $\varepsilon_p$ is the matrix pore strain, dimensionless; $V_p$ represents the pore volume, $m^3$; $\sigma$ is the rock matrix volume stress, Pa; $K_p$ is the matrix pore elastic modulus, Pa; $K_s$ represents the matrix skeleton elastic modulus, Pa.

Matrix porosity is defined as the ratio of matrix pore volume to rock apparent volume:

$$\varphi = \frac{V_p}{V_b} \tag{41}$$

Derive both ends of eq 41, and we can get the following equation (eq 42):

$$d\varphi = d\left(\frac{V_p}{V_b}\right) = \frac{dV_p}{V_b} - \frac{V_p\, dV_b}{V_b^2} = \frac{V_p}{V_b}\left(\frac{dV_p}{V_p} - \frac{dV_b}{V_b}\right) \tag{42}$$

Equations 39−41 are brought into eq 42, and then, the equation can be rewritten as

$$\frac{d\varphi}{\varphi} = \left(\frac{1}{K} - \frac{1}{K_p}\right)(d\sigma - \alpha\, dp) \tag{43}$$

Integrate the porosity, overburden stress, and pore pressure at both ends of eq 43, respectively, and we can get the following equation (eq 44):

$$\varphi = \varphi_0 \exp\left[\left(\frac{1}{K} - \frac{1}{K_p}\right)\left[(\sigma - \sigma_0) - \alpha(p - p_0)\right]\right] \tag{44}$$

where $\varphi_0$ is the initial porosity of the rock matrix, dimensionless; $\varphi$ is the matrix porosity under any pressure condition, dimensionless; $\sigma_0$ refers to the matrix initial stress, Pa; $p_0$ is the initial pore pressure of the matrix, Pa.

Pan and Connell[49] proposed the permeability−porosity cubic law to characterize the evolution of the intrinsic permeability of tight shale rocks with changes in porosity:

$$\frac{k}{k_0} = \left(\frac{\varphi}{\varphi_0}\right)^3 \tag{45}$$

where $k_0$ is the initial permeability of the rock matrix, $m^2$; $k$ is the matrix permeability under any pressure condition, $m^2$.



https://doi.org/10.1021/acsomega.4c09681
ACS Omega 2025, 10, 6948−6964

Therefore, the expression for the shale matrix permeability with respect to pore stress is shown in eq 46:

$$k = k_0 \exp\left[-\frac{3}{K_p}\left[\left(\sigma - \sigma_0\right) - \alpha\left(p - p_0\right)\right]\right] \tag{46}$$

In unconventional reservoir mechanics problems, to facilitate calculation, volume deformation is usually simplified to a uniaxial strain. Assuming that the research unit is infinite, the corresponding horizontal strain is assumed to be zero, that is, $\varepsilon_{22} = \varepsilon_{33} = 0$; the overlying rock pressure is constant, $\sigma_{11}$ = const. Then, eq 34 can be simplified to the expressions of horizontal stress in the other two main directions:

$$\sigma_{22} = \sigma_{33} = \frac{\nu\sigma_{11}}{1-\nu} + \frac{1-2\nu}{1-\nu}(p + K\varepsilon_s) \tag{47}$$

At this moment, the average compressive stress and its increment acting on the matrix unit body are

$$\sigma = \frac{\sum \sigma_{ii}}{3} = \frac{1+\nu\sigma_{11}}{3(1-\nu)} + \frac{2(1-2\nu)}{3(1-\nu)}(p + K\varepsilon_s) \tag{48}$$

$$\mathrm{d}\sigma = \sigma - \sigma_0 = \frac{2(1-2\nu)}{3(1-\nu)}[K(\varepsilon_s - \varepsilon_{s0}) + (p - p_0)] \tag{49}$$

Substituting eq 39 into eq 44 and eq 46, we can get the mathematical expressions of matrix permeability with respect to pore pressure and adsorption expansion strain:

$$k = k_0 \exp\left[\frac{3}{K_p}\left(\frac{\nu+1}{3(1-\nu)}\left(p - p_0\right) - \frac{2E}{9(1-\nu)}\left(\varepsilon_s - \varepsilon_{s0}\right)\right)\right] \tag{50}$$

**2.3. Model Implementation.** Figure 5 depicts the numerical solution process of the salt−water two-phase imbibition coupled rock deformation differential equations. First, a semi-implicit numerical method is used to solve the matrix solute salinity, and then, the water saturation in the rock is explicitly solved. The original nonlinear algebraic partial differential equation and its initial and boundary conditions are discretized into a linear difference equation to form a discrete equation matrix form; see the following equations (eqs 51−64); Moreover, the model convergence time step $\Delta t$ and space step $\Delta x$ are calculated to ensure the convergence of the equation. The spatial area and running time were discretized into M*N grids, and then, the initial water saturation, ion salinity, and pressure were assigned to each spatial grid; What is more, discrete boundary conditions and the initial conditions were combined, and the spatial distribution of water saturation and salinity in the matrix under the influence of stress field changes were solved; Last but not least, if the calculation results are convergent, the computed values will be used as the initial value for the next time step calculation. Otherwise, step 3 must be repeated until the output result at the former moment converges; the last step is to detect the model running time. If the estimated computation time is reached, the program ends, and the calculation results for each time step are generated. If not, then, return to step 3 for calculation of the next time step.

The water−salt-phase discretized differential equation and auxiliary conditions for the imbibition process are as follows:

For the space from 2 to N-1 grids, the water phase difference equation is

$$(\rho_w\varphi)_i^n \frac{S_{wi}^{n+1} - S_{wi}^n}{\Delta t} + \left[\frac{x_c\rho_s m_L (R_L + cR_h^2)}{((R_L + R_h)(1 - cR_h))^2}\frac{\partial R_h}{\partial S_w}\right]_i^n$$
$$\frac{S_{wi}^{n+1} - S_{wi}^n}{\Delta t} = \frac{a_{i-1/2}^n S_{wi-1}^{n+1}}{(\Delta x)^2} + \frac{a_{i+1/2}^n S_{wi+1}^{n+1}}{(\Delta x)^2} - \left(\frac{a_{i-1/2}^n}{(\Delta x)^2} + \frac{a_{i+1/2}^n}{(\Delta x)^2}\right)S_{wi}^{n+1} \tag{51}$$

where the water phase transfer term is a nonlinear function of the water phase relative permeability and pressure, which can be expressed as

$$a = -\rho_w \frac{k k_{rw}}{\mu_w}\frac{\partial(p_w - p_a - p_d)}{\partial S_w} \tag{52}$$

The mass transfer term is calculated using the pressure and water phase saturation at the previous time step. For strong nonlinear items such as relative permeability and capillary force, single-point upstream weighting is used; other parameters involving grid junctions are calculated using the harmonic average. Therefore, the water phase mass transfer term at the grid junction is

$$a_{i\pm1/2}^n = \frac{2a_i^n a_{i\pm1}^n}{a_i^n + a_{i\pm1}^n} \tag{53}$$

For the first spatial grid (outer boundary conditions):

$$S_{w1}^n = S_{wm} \tag{54}$$

For the $N$-th spatial grid (inner boundary conditions):

$$\frac{(S_w)_N^{n+1} - (S_w)_{N-1}^{n+1}}{\Delta x} = 0 \tag{55}$$

Initial conditions for each spatial grid:

$$(S_w)_i^1 = S_{w0} \tag{56}$$

The cumulative volumetric water absorption for the matrix at different imbibition times is given by eq 57:

$$W = \int_0^L A\phi(S_w - S_{w0})\,\mathrm{d}x \tag{57}$$

where $W$ is the total water content imbibed by the shale matrix, $m^3$.

By deriving both ends of eq 57, the matrix water absorption rate can be obtained, as shown in eq 58:

$$q = \frac{\mathrm{d}W}{\mathrm{d}t} \tag{58}$$

where $q$ represents the water imbibition rate, $m^3/s$.

Similarly, for the space grid from 2 to N-1 grid, the difference equation of salt-phase discretization is displayed as

$$(\phi c)_i^n \frac{S_{wi}^{n+1} - S_{wi}^n}{\Delta t} + (\phi S_w)_i^n \frac{c_i^{n+1} - c_i^n}{\Delta t} = \frac{b_{i-1/2}^n c_{i-1}^{n+1}}{(\Delta x)^2} + \frac{b_{i+1/2}^n c_{i+1}^{n+1}}{(\Delta x)^2} - \left(\frac{b_{i-1/2}^n}{(\Delta x)^2} + \frac{b_{i+1/2}^n}{(\Delta x)^2}\right)c_i^{n+1} \tag{59}$$

where it is proposed that the salt-phase conduction term is expressed as a function of the ion diffusion coefficient and membrane efficiency. The expression is



https://doi.org/10.1021/acsomega.4c09681
ACS Omega 2025, 10, 6948−6964

$$b = (1 - n)\phi D_0 \tag{60}$$

The salt-phase mass transfer term at the grid junction is calculated as the harmonic average of each grid parameter at the previous time step:

$$b_{i\pm1/2}^{n} = \frac{2b_i^n b_{i\pm1}^n}{b_i^n + b_{i\pm1}^n} \tag{61}$$

For the first spatial grid (outer boundary conditions):

$$c_1^n = 0 \tag{62}$$

For the $N$-th spatial grid (inner boundary conditions):

$$\frac{c_N^{n+1} - c_{N-1}^{n+1}}{\Delta x} = 0 \tag{63}$$

Initial conditions for each spatial grid:

$$c_i^1 = c_0 \tag{64}$$

## 3. MODEL VALIDATION

We conducted one-dimensional water imbibition physical simulation under geological temperature conditions of 300 K using low-field high pressure gradient nuclear magnetic resonance and an online displacement monitoring method. It was used to characterize how water flows further into a certain shale matrix core. Prior to the experiment, we would saturate the core with nitrogen gas to simulate the initial subsurface gas reservoir conditions. To illustrate how the displacement pressure promotes water imbibition on the core side, we would upload the water pressure on the inlet side and form a positive pressure difference to drive water deeper into the core. Finally, we obtained the water spatial distribution within the core matrix along the imbibition direction and the accumulative water amount at different times.

The experimental data of water imbibition within a certain shale core are used to validate the model reliability throughout historical matching. Based on this model, the water saturation distribution, water imbibition distance, and matrix petrophysical property alteration at different stages were predicted. The adopted model parameters are shown in Table 1, which are from the experimental core data and historically inverted data (labeled as symbol *)

**Table 1. Model Parameters Used in the One-Dimensional Water Imbibition Coupled with the Geomechanical Model**

| parameter | value | parameter | value |
|---|---|---|---|
| core diameter (m) | 0.025 | core length (m) | 0.0682 |
| matrix permeability (mD) | 0.000654 | matrix porosity | 0.0339 |
| clay mineral content | 0.347 | water vicosity (mPa·s) | 1 |
| initial water saturation | 0.001 | equivalent salt concentration (ppm)* | 6000 |
| end point of water phase relative permeability | 0.60 | end point of salt-phase relative permeability | 0.31 |
| injection pressure difference (MPa) | 35 | experimental temperature (K) | 300 |
| imbibition duration (h) | 396 | rock initial elastic modulus (GPa) | 20 |
| clay semipermeable membrane efficiency* | 0.15 | water diffusion coefficient ($m^2/s$)* | 1.6e-9 |
| rock density ($kg/m^3$) | 2600 | Poisson's ratio | 0.21 |

It can be seen from Figure 6 that comprehensively considering capillary force, osmotic pressure, water adsorption

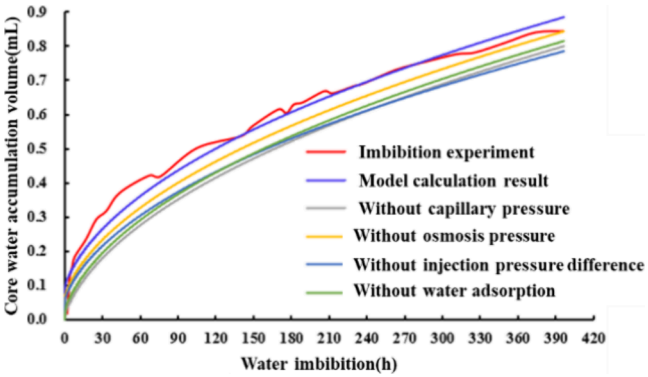


**Figure 6.** Shale core water accumulation volume with respect to time by different models.

onto the clay, and injection pressure difference, the tendency curve calculated by the numerical model is generally consistent with the shale core water imbibition experimental curve with a fitting effect of more than 85%. It could be used to validate the accuracy of the water imbibition model.

As depicted in Figure 7, when the model does not consider any water invasion mechanisms, the cumulative water inflow

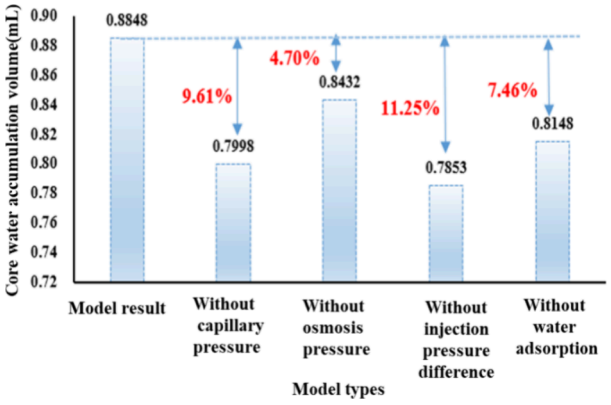


**Figure 7.** Comparison of the ultimate cumulative water accumulation volume calculated by different models.

and water inflow rates of shale are significantly reduced. In addition, when capillary force is not considered in the model, the calculated cumulative water imbibition volume of the core is 0.7998 mL, which is 9.61% lower than the numerical model proposed in this paper. What is more, the cumulative water imbibition amount estimated by the model without considering osmotic pressure is confirmed to be 4.70% lower than the numerical simulation results. Meanwhile, if the model includes the injection pressure difference, in other words, the water imbibition belongs to the forced imbibition process, the calculation result is about 11.25% higher than the accumulated spontaneous water intrusion amount. Additionally, when the clay water adsorption mechanism is not considered in the core water imbibition process, the imbibed water accumulation within the shale core is reduced by 7.46%. In summary, the more comprehensive the water imbibition mechanisms included in the numerical simulation in this paper, the higher the accuracy of predicting the water imbibition process within



https://doi.org/10.1021/acsomega.4c09681
ACS Omega 2025, 10, 6948−6964

shale cores, which is conducive to carry out accurate analysis in the correlation between water imbibition and stress-sensitive flow capacity of shale cores.

Core water invasion is affected by capillary force, osmotic pressure, and injection pressure difference (Figure 8). Capillary

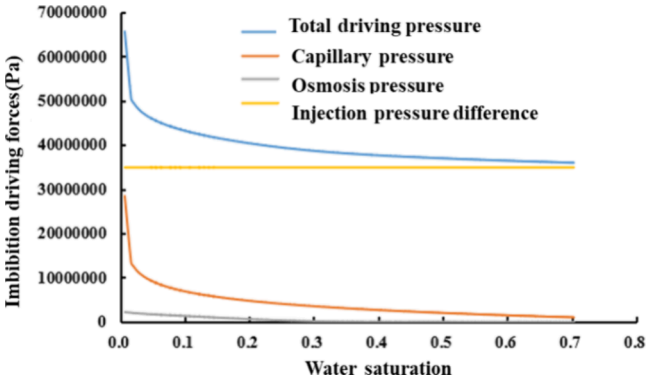


**Figure 8.** Correlation curve between the shale core water invasion driving force and water saturation.

force and osmotic pressure are negatively correlated with water saturation: as water saturation increases, the difference in salinity inside and outside the core gradually becomes smaller, and therefore, the osmotic pressure dynamic decreases. Meanwhile, under the action of water invasion driving forces, the water saturation in the core gradually increases until the water saturation difference inside and outside becomes zero. Thereafter, the decline in the capillary pressure leads to a decrease in the driving forces for the water imbibition process.

As displayed in Figure 9, the water saturation profile spreads in a funnel shape to the central core away from the water

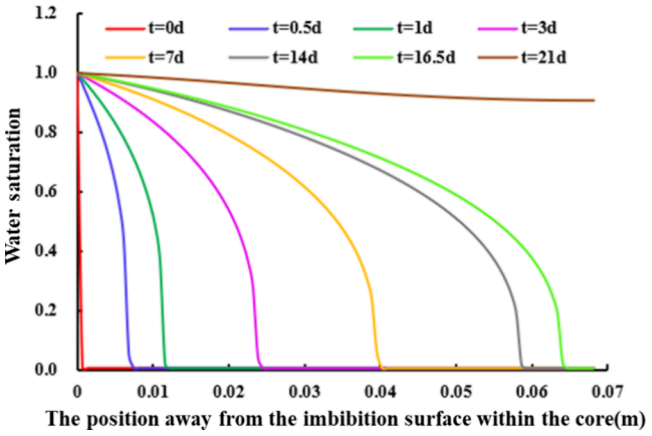


**Figure 9.** Shale core water saturation distribution profiles at different durations

imbibition end face of the core. The water saturation decreases significantly as the distance away from the core imbibition end increases: as the imbibition lasts for 12 h, the water imbibition distance is less than 0.01 m. At 1 week of imbibition duration, the water imbibition thickness is calculated to be 0.04 m. At the end of the experiment (16.5 days), the rock is not completely water invaded. Not until 21 days after imbibing water is the rock fully water invaded and the core average water saturation is basically distributed above 0.9. As shown in Figure 10, the salt concentration inside the core increases with the

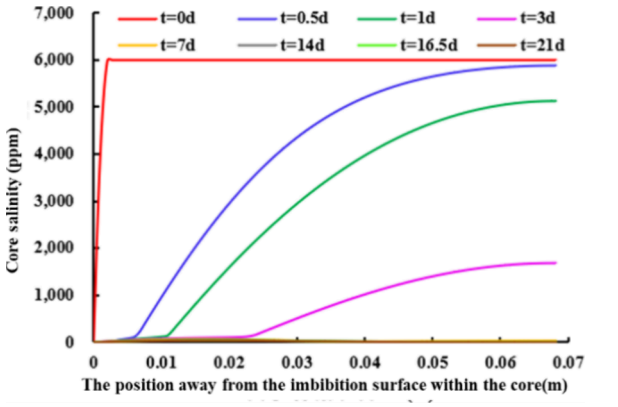


**Figure 10.** Shale core salinity profile distribution curves at different durations.

imbibition distance within the matrix, and the solution concentration inside the core is negatively correlated with the imbibition duration: when the water imbibition time is 1 week, the salinity inside the core is basically 0. It is calculated by the model that the rock water imbibition distance increases in the form of a power function law as the water duration time goes up (Figure 11). When the water duration time reaches 17.20 days, the rock water just fully saturates the rock.

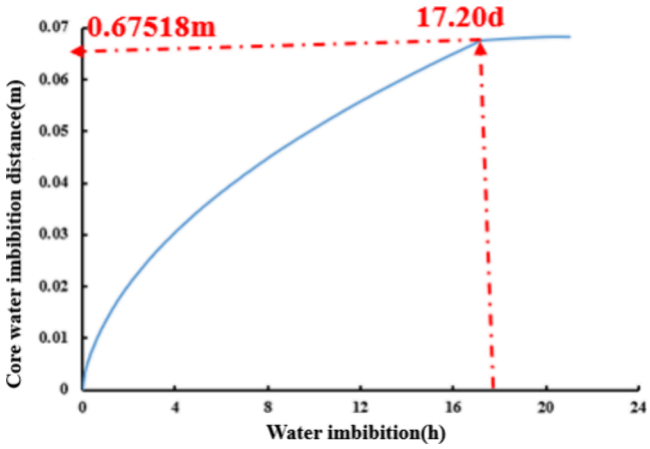


**Figure 11.** Correlation chart between core water imbibition depth versus imbibition duration.

It can be seen from Figures 12 and 13 that the higher the water saturation inside the rock, the higher the elastic modulus decreases exponentially. When the water saturation increases from 0 to 0.7, the elastic modulus decreases by 6.96%. This is due to the water imbibition inside the rock, the core average water saturation increases and further can be converted into water vapor affected by relative pressure, leading to an increase in the relative humidity. Moreover, strong forces such as hydrogen bonds between the adsorbed water vapor molecules and the clay mineral particles, as well as the generated double electric layer repulsion, all promote the increase in the distance between the double electric layers of clay and result in the clay minerals' macroscopic swelling deformation, strengthening the reduction in the cementation between solid rock particles and thus weakening the elastic modulus.

As seen in Figure 14, the stress sensitivity after hydration is higher than that before hydration: the core permeability after hydration decreases exponentially from $3.16 \times 10^{-4}$ mD to



https://doi.org/10.1021/acsomega.4c09681
ACS Omega 2025, 10, 6948−6964

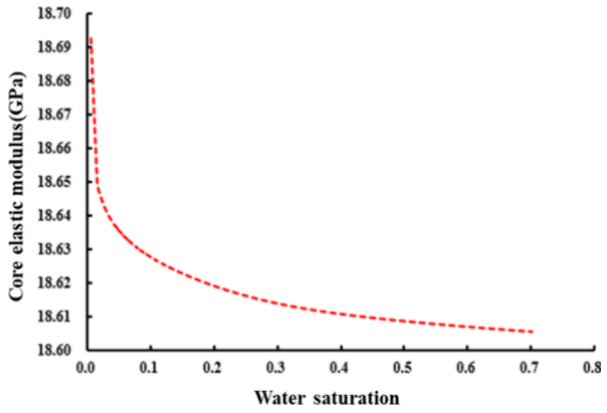


**Figure 12.** Changes of the shale core elastic modulus with water saturation.

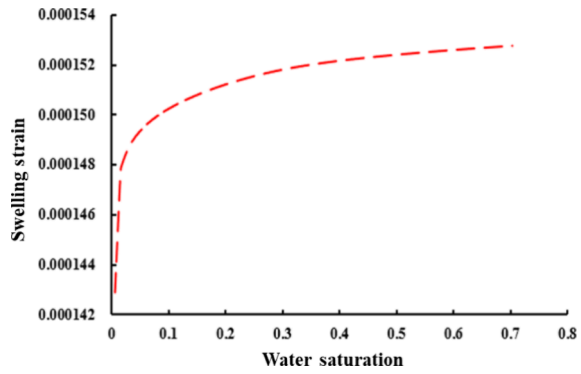


**Figure 13.** Curve of shale core swelling strain with respect to water saturation.

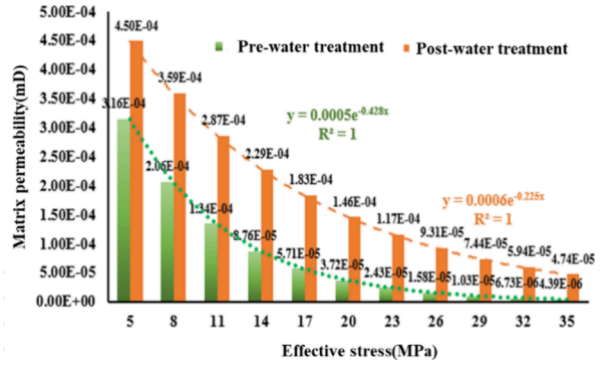


**Figure 14.** Diagram of shale core permeability sensitive to effective pressure.

$4.39 \times 10^{-6}$ mD. The stress sensitivity coefficient by fitting is 0.428 $MPa^{-1}$; after hydration, the core permeability decreases from $4.50 \times 10^{-4}$ to $4.74 \times 10^{-5}$ mD, and the stress sensitivity coefficient is 0.225 $MPa^{-1}$.

## 4. RESULTS AND DISCUSSION

**4.1. Impact of Initial Matrix Permeability on Shale Water Imbibition.** As indicated from Figure 15, the higher the initial matrix permeability, the higher the water imbibition accumulation volume.

There is an exponential positive correlation between the shale water imbibition distance and the initial matrix permeability (as seen in Figure 16): the greater the initial matrix permeability, the larger the water flow capacity in the

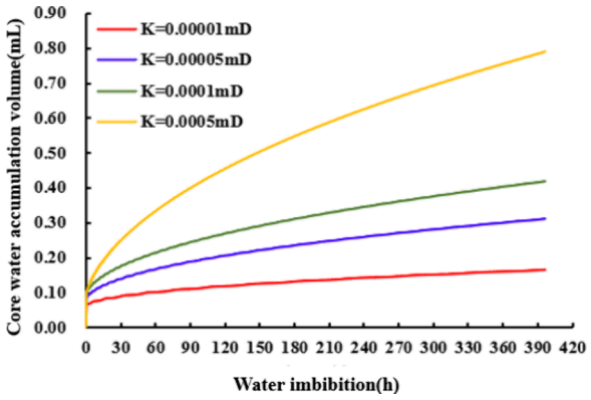


**Figure 15.** Variation of core water accumulation volume with imbibition duration under different matrix permeabilities.

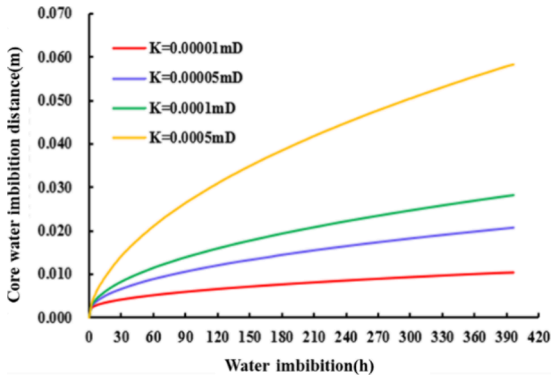


**Figure 16.** Correlation curves between core water imbibition distance and imbibition duration for different matrix permeabilities.

core and the lower the viscous resistance, indicating that water can easily enter the rock, causing a great thickness in rock water invasion. When the matrix permeability increases by 50 times, the rock water invasion thickness increases by 4.61 times. Meanwhile, it can be confirmed from Figure 17 that the

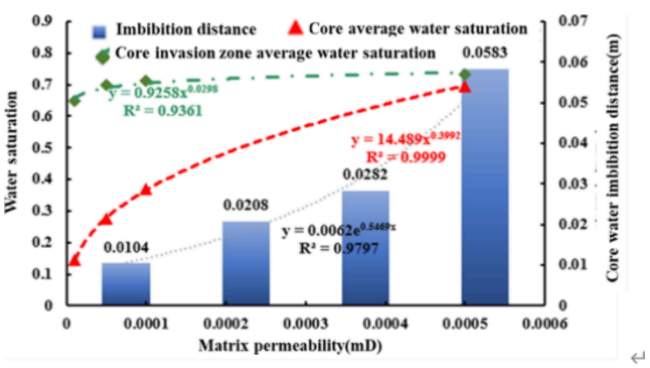


**Figure 17.** Changes in core water saturation and water imbibition distance with respect to matrix permeability.

core water saturation increases with the matrix permeability, which meets a power function law: if the matrix permeability increases from 0.00001 to 0.0005 mD, the average water saturation increases from 0.146 to 0.697. As a result, the matrix permeability increased by 50 times, and the average core water saturation increased by 5 times.

Figures 18 and 19 confirmed that water adsorption in shale clay minerals triggers matrix swelling deformation. The cores



https://doi.org/10.1021/acsomega.4c09681
ACS Omega 2025, 10, 6948−6964

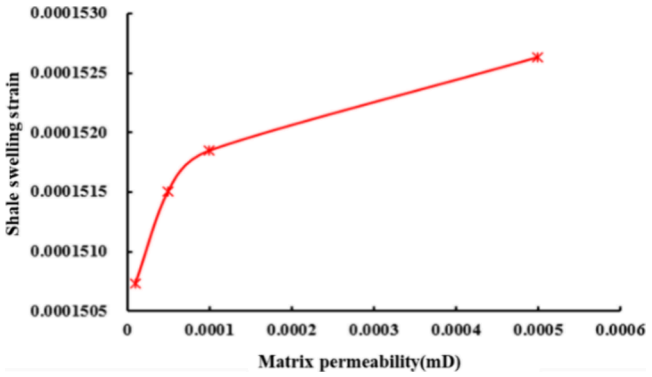


**Figure 18.** Curve of core swelling strain versus matrix permeability.

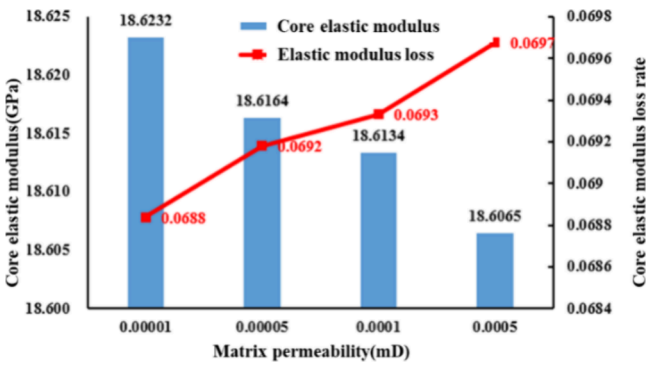


**Figure 19.** Relationship curves of shale elastic modulus and its loss rate with respect to the matrix permeability.

with higher initial matrix permeability cause obvious shale swelling deformation in the form of a power function law, inducing a significant decrease in the shale elastic modulus. This is because the higher the matrix permeability, the higher the water content absorbed by the core per unit time, leading to shale clay swelling and thus weakening the rock cementation significantly. As a result, when the matrix permeability increases from 0.00001 to 0.0005 mD, the hydrated rock elastic modulus will decrease by 6.97%. It can be seen from Figure 20 that the permeability of cores with different initial matrix permeabilities decreases exponentially with the growth in effective stress, and the stress sensitivity coefficient before hydration and post hydration remains basically unchanged,

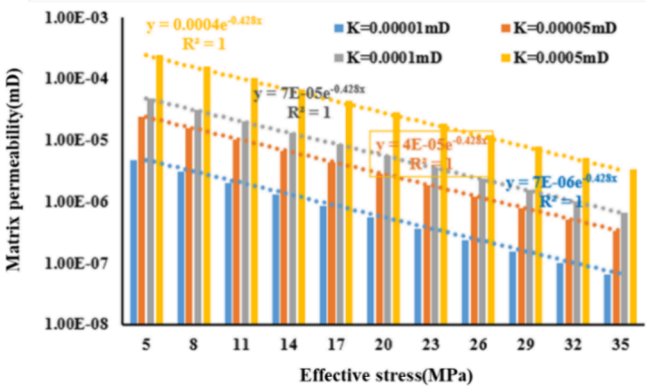


**Figure 20.** Diagram of shale core permeability sensitive to effective pressure at different matrix permeabilities.

indicating that the initial matrix permeability has no direct relationship with the stress sensitivity coefficient.

**4.2. Impact of Clay Mineral Content on Shale Water Imbibition.** As depicted in Figure 21, the cumulative water volumes for shale rocks are positively correlated with the clay mineral content.

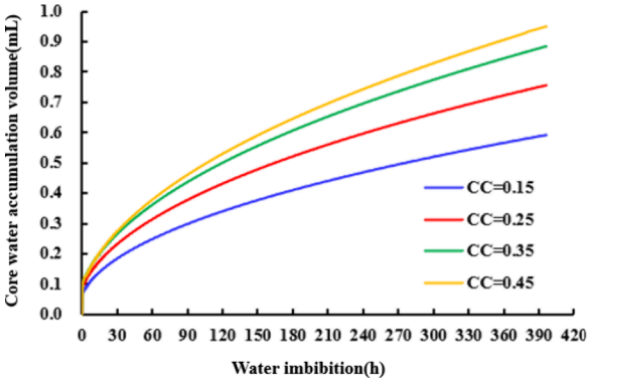


**Figure 21.** Curves of core water accumulation volume with imbibition duration under different clay mineral contents.

Figures 22 and 23 show that the core water imbibition distance increases in the form of the power function law as the

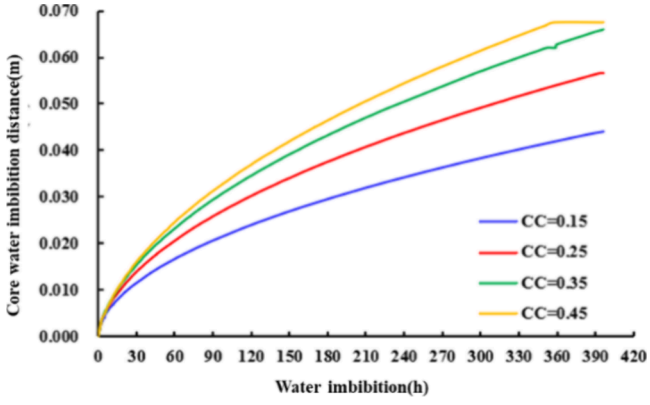


**Figure 22.** Correlation curves between core water imbibition distance and imbibition duration for different clay mineral contents.

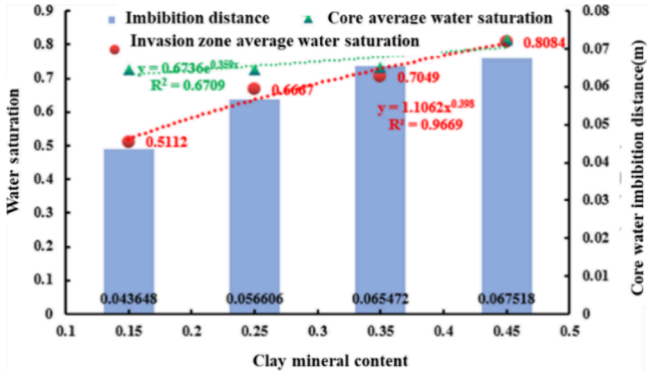


**Figure 23.** Changes in core water saturation and water imbibition distance with respect to clay mineral contents.

clay mineral content increases: the higher the clay mineral content, the greater the number of multilayer adsorption sites for water vapor in the clay particles. Within the same



https://doi.org/10.1021/acsomega.4c09681
ACS Omega 2025, 10, 6948−6964

imbibition time, water saturation has a positively exponential correlation with adsorbed water content, and therefore, the relative humidity linearly increases with water saturation. As a result, the amount of adsorbed water per unit mass of clay mineral particles shows a logarithmic growth trend as the clay mineral content increases, resulting in the greater thickness of the rock water invasion. When the clay mineral content increases from 0.15 to 0.45, the average water saturation increases by 58.12%, and the rock water invasion thickness increases from 0.0436 to 0.0675 m, an increase of 54.82%.

It can be seen from Figure 24 and Figure 25 that the higher the clay mineral content in the core, the more multilayer

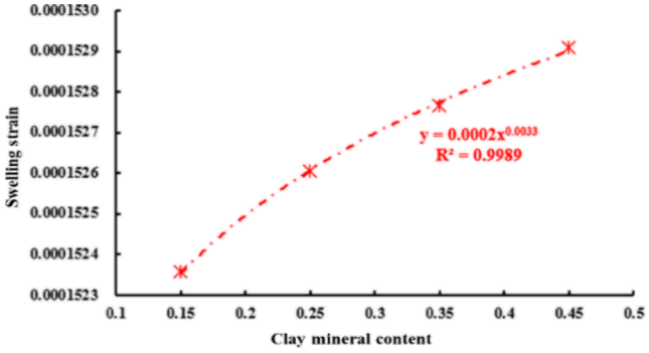


**Figure 24.** Curve of core swelling strain vs clay mineral contents.

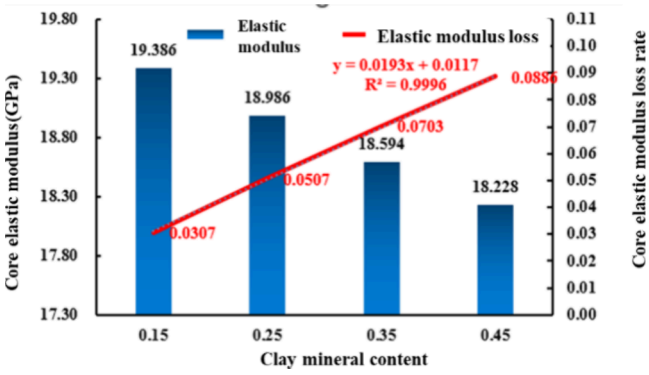


**Figure 25.** Relationship curves of the shale elastic modulus and its loss rate with respect to the clay mineral contents.

adsorption of water vapor on the surface of the clay mineral particles and the greater the amount of adsorbed water per unit mass of rock, which promotes the growth of the matrix expansion deformation. When the clay mineral content increases from 0.15 to 0.45, the elastic modulus loss rate of shale after hydration increases from 3.07 to 8.86%.

It can be seen from Figure 26 that the higher the clay mineral content is, the higher the stress sensitivity coefficient. When the clay mineral content increases from 0.15 to 0.45, the stress sensitivity coefficient increases from 0.412 to 0.434 $MPa^{-1}$, and the core permeability loss rate after hydration is proportional to the clay mineral content. There is a linear negative correlation between matrix permeability and swelling deformation (Figure 27): the higher the clay mineral content, the more water molecule layers adsorbed on the surface of clay mineral particles and the more obvious the core swelling deformation, which affects the matrix permeability more significantly.

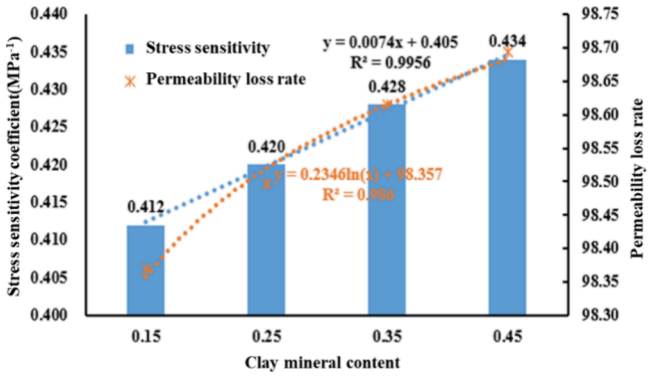


**Figure 26.** Correlation chart between core stress sensitivity coefficient and permeability loss rate with respect to clay mineral contents.

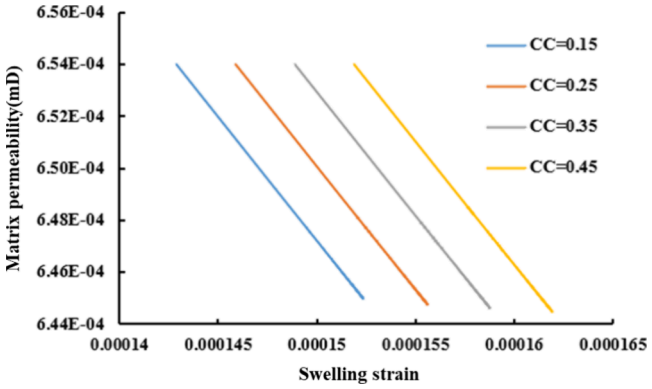


**Figure 27.** Correlation curves between core matrix permeability and swelling strain with different clay mineral contents.

**4.3. Impact of Injection Pressure Difference on Shale Water Imbibition.** The cumulative water volume of the rock is positively correlated with the injection pressure difference (Figure 28).

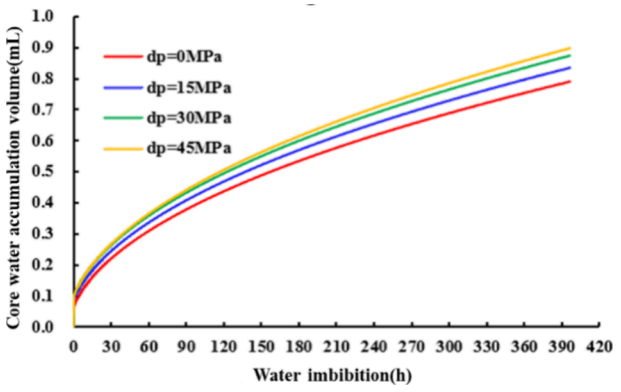


**Figure 28.** Curves of core water accumulation volume with imbibition duration under different injection pressure differences.

Figure 29 indicates that the higher the core injection pressure difference, the more the rock water invasion thickness increases linearly since a higher injection pressure difference is applied to the shale water invasion end face, and thus, more adsorbed water enters the interior rock, leading to a linear increase in water saturation (Figure 30). As indicated in Figure 31, during the shale water imbibition process, multiple layered water molecules are adsorbed within the shale clay mineral



https://doi.org/10.1021/acsomega.4c09681
ACS Omega 2025, 10, 6948−6964

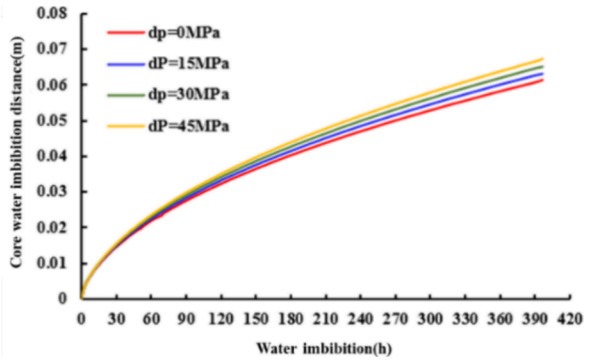


**Figure 29.** Correlation curves between core water imbibition distance and imbibition duration for different injection pressure differences.

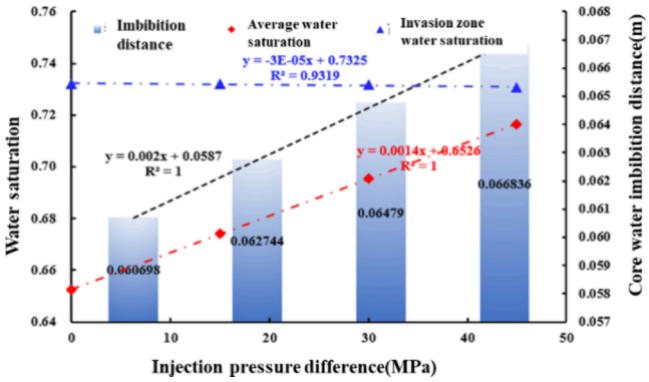


**Figure 30.** Changes in core water saturation and water invasion depth with respect to injection pressure difference.

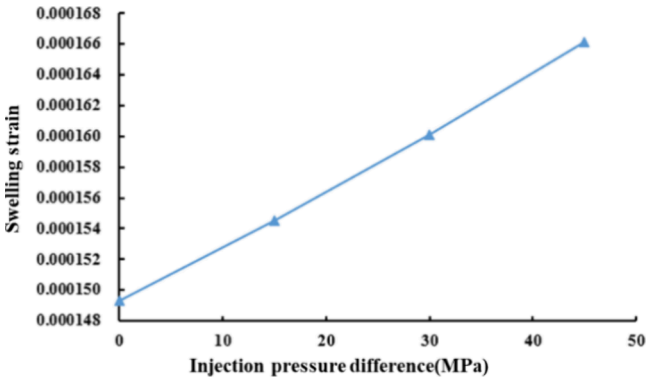


**Figure 31.** Curve of core swelling strain versus injection pressure difference.

particles, triggering clay swelling and shale deformation. The higher the injection pressure difference, the shale expansion and deformation generally increase linearly.

It is found that the elastic modulus of shale has a negative correlation with the core injection pressure difference. As shown in Figure 32, the greater the injection pressure difference, the greater the amount of adsorbed water per unit mass of rock, and thus, the shale deformation caused by clay swelling increases linearly and the rock cementation is significantly weakened: when the injection pressure difference increases from 0 to 45 MPa, the elastic modulus of the shale after hydration decreases from 6.83 to 7.56%. As seen in Figure 33 and Figure 34, the greater the injection pressure difference, the higher the stress sensitivity coefficient. When the injection pressure difference increases from 0 to 45 MPa, the stress

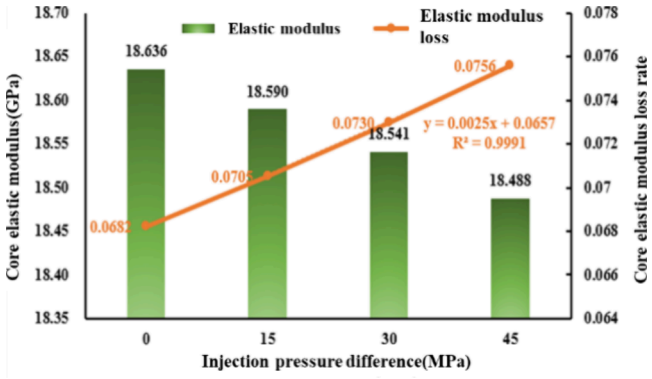


**Figure 32.** Relationship curves of shale elastic modulus and its loss rate with respect to the injection pressure difference.

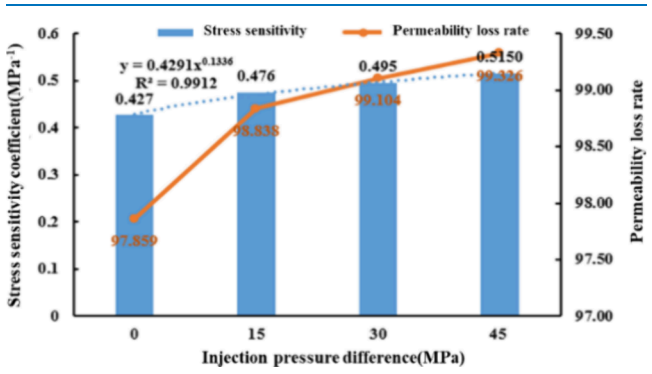


**Figure 33.** Correlation chart between core stress sensitivity coefficient and permeability loss rate with respect to injection pressure difference.

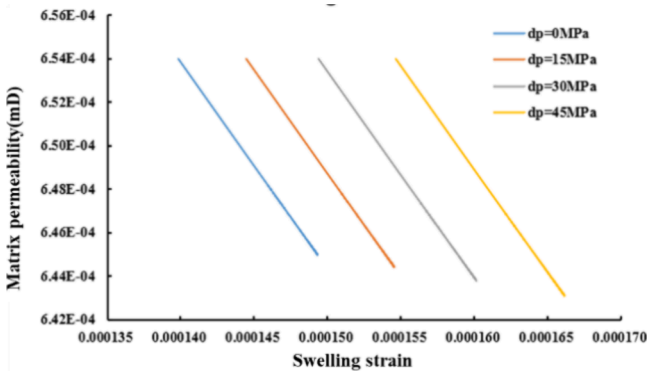


**Figure 34.** Comparison of correlation curves between core matrix permeability and swelling strain at different injection pressure differences.

sensitivity coefficient increases from 0.412 to 0.434 $MPa^{-1}$, and the permeability loss rate is proportional to the injection pressure difference. This is because the larger the core injection pressure difference, the more water intrudes into the core, which leads to a greater number of water molecules on the surface of clay mineral particles, and further results in the more obvious shale deformation. Ultimately, it occupies the flow channels and pore spaces in the matrix, resulting in a significant reduction in matrix permeability.

## 5. CONCLUSIONS

(1) Water imbibition mechanisms such as capillary force, osmotic pressure, clay adsorption, and water injection



https://doi.org/10.1021/acsomega.4c09681
ACS Omega 2025, 10, 6948−6964

pressure difference are demonstrated to play a crucial role in the water imbibition process within shale matrix, which improve significantly the prediction of water imbibition for gas shale.

(2) A theoretical mathematical relationship was established between water imbibition thickness with respect to imbibition duration, initial matrix permeability, clay mineral content, and injection pressure difference. It is found that water imbibition distance is a power function of water imbibition duration.

(3) The elastic modulus after hydration is negatively related to the matrix permeability, clay mineral content, and injection pressure difference. These bigger control factors will trigger more water entering matrix and further result in clay swelling caused by water adsorption and weakening cementation of solid shale, finally enhancing the stress sensitivity and inducing the loss in the permeability.

(4) The theoretical mathematical expression of hydration stress sensitivity related to the clay mineral content, water saturation, and injection pressure difference is directly established. The stress sensitivity coefficient of cores with different initial matrix permeabilities is basically unchanged; the higher the clay mineral content, the higher the stress sensitivity coefficient; the stress sensitivity coefficient has a positive power function of the injection pressure difference.

## ■ ASSOCIATED CONTENT

### Data Availability Statement

The data that supports the findings of this study are not available for now due to the ongoing project. Otherwise, it can be accessible from the corresponding author upon reasonable request.

## ■ AUTHOR INFORMATION


### Corresponding Author

**Yingying Xu** − *Research Institute of Petroleum Exploration and Development, PetroChina, Beijing 100083, China;* orcid.org/0000-0001-8224-2342; Email: xuyy0329@foxmail.com

### Authors

**Kaifu Mi** − *Beijing Petroleum Machinery Co., Ltd., Beijing 102206, China*

**Yu Lei** − *Beijing Petroleum Machinery Co., Ltd., Beijing 102206, China*

**Juncheng Wang** − *Beijing Petroleum Machinery Co., Ltd., Beijing 102206, China*

**Pengyu Shen** − *Beijing Petroleum Machinery Co., Ltd., Beijing 102206, China*

**Xueming Zhang** − *Beijing Petroleum Machinery Co., Ltd., Beijing 102206, China*

Complete contact information is available at: https://pubs.acs.org/10.1021/acsomega.4c09681


### Author Contributions

Kaifu Mi: conceptualization, methodology, writing-original draft, project administration; Yingying Xu: conceptualization, methodology, writing-original draft, writing-reviewing and editing; Yu Lei: resources, investigation; Juncheng Wang: resources, investigation; Pengyu Shen: resources, investigation; Xueming Zhang: resources, investigation.

### Notes

The authors declare no competing financial interest.

## ■ ACKNOWLEDGMENTS

This research was funded by the Major Engineering Technology Field Testing Project of PetroChina "Onsite Test of Key Equipment and Automation Control System for Shale Gas Testing and Gas Production Integration" (grant no. 2022ZS05).

## ■ REFERENCES


(1) Chen, T.; Fu, Y.; Feng, X.; Tan, Y.; Cui, G.; Elsworth, D.; Pan, Z. Gas permeability and fracture compressibility for proppant-supported shale fractures under high stress. *J. Nat. Gas Sci. Eng.* **2021**, *95*, No. 104157.

(2) Liu, Z.; Pan, Z.; Li, S.; Zhang, L.; Wang, F.; Han, L.; Zhang, J.; Ma, Y.; Li, H.; Li, W. Study on the effect of cemented natural fractures on hydraulic fracture propagation in volcanic reservoirs. *Energy* **2022**, *241*, No. 122845.

(3) Zhou, H.; Liu, X.; Chen, M.; et al. Effects of fracturing fluid migration with clay damage after different shut-in period on shale gas production performance[J]. *Energy Reports* **2022**, *8*, 4265−4273.

(4) Li, R.; Wang, M.; Wang, R.; et al. Sensitivity and application of pseudo-steady-state constant for refracturing horizontal wells with fracture reorientation in anisotropic tight oil reservoirs. *Unconv. Resour.* **2023**, *3*, 123−133.

(5) Liao, K.; Zhu, J.; Sun, X.; et al. Numerical Investigation on Injected-Fluid Recovery and Production Performance following Hydraulic Fracturing in Shale Oil Wells[J]. *Processes* **2022**, *10* (9), 1749.

(6) Wang, X.; Wang, S.; Wu, W.; et al. Coupled pressure-driven flow and spontaneous imbibition in shale oil reservoirs. *Phys. Fluids* **2023**, *35* (4), No. 042104.

(7) Alipour, K. M.; Kasha, A.; Sakhaee-Pour, A.; et al. Empirical Relation for Capillary Pressure in Shale. *Petrophysics* **2022**, *63* (5), 591−603.

(8) Cheng, H.; Wang, F. Mathematical model of the spontaneous imbibition of water into oil-saturated fractured porous media with gravity[J]. *Chem. Eng. Sci.* **2021**, *231*, No. 116317.

(9) Zhou, Y.; Guan, W.; Zhao, C.; et al. Spontaneous imbibition behavior in porous media with various hydraulic fracture propagations: A pore-scale perspective. *Adv. Geo-Energy Res.* **2023**, *9* (3), 185−197.

(10) Mohammadmoradi, P.; Kantzas, A. Modelling shale spontaneous water intake using semi-analytical and numerical approaches[J]. *Canadian Journal of Chemical Engineering* **2019**, *97*, 1627−1642.

(11) Marine, I. W.; Fritz, S. J. Osmotic model to explain anomalous hydraulic heads. *Water Resour. Res.* **1981**, *17* (1), 73−82.

(12) Yang, L.; Wang, H.; Xu, H.; et al. Experimental study on characteristics of water imbibition and ion diffusion in shale reservoirs[J]. *Geoenergy Science and Engineering* **2023**, *229*, No. 212167.

(13) Hu, J.; Zhao, H.; Du, X.; et al. An analytical model for shut-in time optimization after hydraulic fracturing in shale oil reservoirs with imbibition experiments[J]. *J. Pet. Sci. Eng.* **2022**, *210*, No. 110055.

(14) Li, S.; Liu, W.; Zhang, H.; Xiao, H. Experimental study of spontaneous imbibition in low-permeability reservoir. *Acta Pet. Sin.* **2007**, 109−112.

(15) Pu, Y.; Wang, X. Y.; Yang, S. Research on spontaneous imbibition mechanism of tight oil reservoirs using NMRI method. *J. Petrochem. Univ.* **2017**, *1* (53), 45−48.

(16) Akin, S.; Kovscek, A. R. Imbibition Studies of Low-Permeability Porous Media, In *SPE Western Regional Meeting*, **1999**.




https://doi.org/10.1021/acsomega.4c09681
*ACS Omega* 2025, 10, 6948−6964

(17) Wang, F. Y.; Yang, K. Influence of pore throat size distribution on oil displacement by spontaneous imbibition in tight oil reser-voirs. *Lithol. Reservoirs* **2021**, *33* (2), 155−162.
(18) Schmid, K. S.; Alyafei, N.; Geiger, S.; Blunt, M. J. Analytical solutions for spontaneous imbibition: fractional-flow theory and experimental analysis. *Spe J.* **2016**, *21* (6), 2308−2316.
(19) Abbasi, J.; Sarafrazi, S.; Riazi, M.; Ghaedi, M. Improvements in scaling of countercurrent imbibition recovery curves using a shape factor including permeability anisotropy. *J. Geophys. Eng.* **2018**, *15* (1), 135−141.
(20) Wang, Z.; Yang, Z.; Ding, Y.; et al. A generalized capillary imbibition model for porous media in tight reservoirs. *Adv. Civil Eng.* **2018**, *2018*, No. 4148734.
(21) Wang, F.; Zhao, J. A mathematical model for co-current spontaneous water imbibition into oil- saturated tight sandstone: Upscaling from pore-scale to core-scale with fractal approach. *J. Pet. Sci. Eng.* **2019**, *178*, 376−388.
(22) Salam, A.; Wang, X. An analytical solution on spontaneous imbibition coupled with fractal roughness, slippage and gravity effects in low permeability reservoir. *J. Pet. Sci. Eng.* **2022**, *208*, No. 109501.
(23) Shun, L.; Jun, N.; Xianli, W.; Xiong, L.; et al. A dual-porous and dual-permeable media model for imbibition in tight sandstone reservoirs. *J. Pet. Sci. Eng.* **2020**, *194*, No. 107477.
(24) Tavassoli, Z.; Zimmerman, R. W.; Blunt, M. J. Analytic analysis for oil recovery during counter-current imbibition in strongly water-wet systems. *Transp. Porous Media* **2005**, *58* (1), 173−189.
(25) Behbahani, H. S.; Di Donato, G.; Blunt, M. J. Simulation of counter-current imbibition in water-wet fractured reservoirs. *J. Pet. Sci. Eng.* **2006**, *50* (1), 21−39.
(26) Sharifigaliuk, H.; Mahmood, S.; Ahmad, M.; Khosravi, V.; Matysek, D. Comparative analysis of conventional methods for the evaluation of wettability in shales. *J. Pet. Sci. Eng.* **2022**, *208*, No. 109729.
(27) Brochard, L.; Vandamme, M.; Pellenq, J. M. Poromechanics of microporous media. *J. Mech. Phys. Solids* **2012**, *60* (4), 606−622.
(28) Wang, L.; Bornert, M.; Héripré, E.; Chanchole, S.; Pouya, A.; Halphen, B. Microscale insight into the influence of humidity on the mechanical behavior of mudstones. *J. Geophys. Res. Solid Earth* **2015**, *120* (5), 3173−3186.
(29) Wu, P.; Li, Y.; Wang, L.; Sun, X.; Wu, D.; He, Y.; Li, Q.; Song, Y. Hydrate-bearing sediment of the South China Sea: microstructure and mechanical characteristics. *Eng. Geol.* **2022**, *307*, No. 106782.
(30) Zhu, W. C.; Wei, C. H. Numerical simulation on mining-induced water inrushes related to geologic structures using a damage-based hydromechanical model. *Environ. Earth Sci.* **2011**, *62* (1), 43−54.
(31) Costin, L. S. A microcrack model for the deformation and failure of brittle rock. *J. Geophys. Res. Atmos.* **1983**, *88* (B11), 9485−9492.
(32) Shao, J. F.; Chau, K. T.; Feng, X. T. Modeling of anisotropic damage and creep deformation in brittle rocks. *Int. J. Rock Mech. Min. Sci.* **2006**, *43* (4), 582−592.
(33) Golshani, A.; Oda, M.; Okui, Y.; Takemura, T.; Munkhtogoo, E. Numerical simulation of the excavation damaged zone around an opening in brittle rock. *Int. J. Rock Mech. Min. Sci.* **2007**, *44* (6), 835−845.
(34) Brantut, N.; Baud, P.; Heap, M. J.; Meredith, P. G. Micromechanics of brittle creep in rocks. *J. Geophys. Res. Solid Earth* **2012**, *117* (B8), 1133−1172.
(35) Liu, K.; Sheng, J. J., "A new experimental methodology to investigate water adsorption into shale under stress anisotropy conditions," In *SPE Liquids-Rich Basins Conference North America*; Society of Petroleum Engineers, 2019.
(36) Mooney, R. W.; Keenan, A. G.; Wood, L. A. Adsorption of Water Vapor by Montmorillonite. II. Effect of Exchangeable Ions and Lattice Swelling as Measured by X-Ray Diffraction[J]. *J. Am. Chem. Soc.* **1952**, *74* (6), 1371−1374.
(37) Powell, D. H.; Fischer, H. E.; Skipper, N. T. The Structure of Interlayer Water in Li−Montmorillonite Studied by Neutron Diffraction with Isotopic Substitution. *J. Phys. Chem. B* **1998**, *102* (52), 10899−10905.
(38) Hensen, E. J. M.; Smit, B. Why Clays Swell. *J. Phys. Chem. B* **2002**, 12664.
(39) Zhang, F.; Low, P. F.; Roth, C. B. Effects of Monovalent, Exchangeable Cations and Electrolytes on the Relation between Swelling Pressure and Interlayer Distance in Montmorillonite-[J].Journal of Colloid &. *Interface Science* **1995**, *173* (1), 34−41.
(40) Furmaniak, S.; Gauden, P. A.; Terzyk, A. P.; Rychlicki, G. Water adsorption on carbons - critical review of the most popular analytical approaches. *Adv. Colloid Interface Sci.* **2008**, *137*, 82−143.
(41) Qu, H.; Peng, Y.; Pan, Z.; et al. A fully coupled simulation model for water spontaneous imbibition into brittle shale. *J. Natural Gas Sci. Eng.* **2019**, *66*, 293−305.
(42) Dehghanpour, H.; Lan, Q.; Saeed, Y.; Fei, H.; Qi, Z. Spontaneous imbibition of brine and oil in gas shales: effect of water adsorption and resulting microfractures. *Energy Fuel.* **2013**, *27* (6), 3039−3049.
(43) Davidson, D. M. *The Van't Hoff Law of Solution*. The University of Chicago, 1909.
(44) Daian, J. F. Condensation and isothermal water transfer in cement mortar Part I ? Pore size distribution, equilibrium water condensation and imbibition. *Transp. Porous Media* **1988**, *3*, 563−589.
(45) SHI, J.; DURUCAN, S. Drawdown induced changes in permeability of coalbeds: a new interpretation of the reservoir response to primary recovery[J]. *Transport in porous media* **2004**, *56* (1), 1−16.
(46) Mian, C.; Zhida, C. Effective stress laws for multi-porosity media[J]. *Applied Mathematics and Mechanics* **1999**, *20*, 1207−1213.
(47) Guiggiani, M.; Gigante, A. A general algorithm for multi-dimensional Cauchy principal value integrals in the boundary element method. *J. Appl. Mech.* **1990**, 906−915.
(48) Hattel, J. H.; Hansen, P. N. A control volume-based finite difference method for solving the equilibrium equations in terms of displacements[J]. *Applied Mathematical Modelling* **1995**, *19* (4), 210−243.
(49) Pan, Z.; Connell, L. D. Modelling permeability for coal reservoirs: a review of analytical models and testing data. *Int. J. Coal Geol.* **2012**, *92*, 1−44.


https://doi.org/10.1021/acsomega.4c09681
*ACS Omega* 2025, 10, 6948−6964